

RESEARCH ARTICLE

10.1002/2015JA021725

Key Points:

- The geomagnetic poles enhance the generation and detection of teleseismic CIDs
- Beamformed apparent velocity and azimuth of CIDs produced by the Maule and Tohoku-Oki earthquakes
- Development of virtual array beamforming of acoustic wave signals inverted from TEC data

Correspondence to:

D. Gómez,
ddgomez@memphis.edu

Citation:

Gómez, D., et al. (2015), Virtual array beamforming of GPS TEC observations of coseismic ionospheric disturbances near the Geomagnetic South Pole triggered by teleseismic megathrusts, *J. Geophys. Res. Space Physics*, 120, doi:10.1002/2015JA021725.

Received 28 JUL 2015

Accepted 24 SEP 2015

Accepted article online 29 SEP 2015

Virtual array beamforming of GPS TEC observations of coseismic ionospheric disturbances near the Geomagnetic South Pole triggered by teleseismic megathrusts

Demián Gómez¹, Robert Smalley Jr.¹, Charles A. Langston¹, Terry J. Wilson², Michael Bevis², Ian W. D. Dalziel³, Eric C. Kendrick², Stephanie A. Konfal², Michael J. Willis⁴, Diego A. Piñón⁵, Sergio R. Cimbaro⁵, and Dana Caccamise²

¹Center for Earthquake Research and Information, The University of Memphis, Memphis, Tennessee, USA, ²School of Earth Sciences, The Ohio State University, Columbus, Ohio, USA, ³Institute for Geophysics, University of Texas at Austin, Austin, Texas, USA, ⁴Earth and Atmospheric Sciences, Cornell University, Ithaca, New York, USA, ⁵Instituto Geográfico Nacional, Buenos Aires, Argentina

Abstract We identified coseismic ionospheric disturbances (CID) in Antarctica generated by the 2010 Maule and the 2011 Tohoku-Oki earthquakes analyzing total electron content (TEC) data with a modified beamforming technique. Beamforming in Antarctica, however, is not straightforward due to the effects of array deformation and atmospheric neutral wave-ionospheric plasma coupling. We take these effects into account and present a method to invert for the seismically generated acoustic wave using TEC observations. The back azimuths, speeds, and waveforms obtained by the beamform are in excellent agreement with the hypothesis that the TEC signals are generated by the passage of Rayleigh waves from the Maule and Tohoku-Oki earthquakes. The Tohoku-Oki earthquake is ~12,500 km from Antarctica, making this the farthest observation of CIDs to date using GPS.

1. Introduction

Vertical ground displacement during seismic activity produce, by dynamic coupling, near- and far-field acoustic and gravity waves that propagate in the neutral atmosphere. As acoustic waves propagate upward, their amplitudes increase by a factor of $\sim 10^4$ in the ionosphere due to energy conservation as the density in the atmosphere decreases. At ionospheric altitudes, neutral particles couple with the ionized plasma perturbing the ionospheric electron density. The ionosphere is dispersive, with the dispersion proportional to the total electron content (TEC), the integrated electron density along the satellite-receiver line of sight (LOS). To correct for the effects of the dispersion, the GPS system uses two frequencies to estimate the TEC. These GPS TEC estimates can also be used to study ionospheric perturbations [Mannucci et al., 1993].

Several authors have studied the propagation of TEC perturbations produced by different sources such as explosions, rocket launches [e.g., Fitzgerald, 1997; Calais and Minster, 1998; Afraimovich et al., 2001], tsunamis [Artru et al., 2005], and earthquakes [Calais and Minster, 1995] that produce a combination of acoustic and gravity waves that may be detected in the ionosphere. These studies have found that the generation and detection of these perturbations in the *F* layer of the ionosphere depend on the orientation of the neutral perturbation with respect to the geomagnetic inclination and the sensitivity of the observational method being used (e.g., GPS, Doppler sounding, and over-the-horizon radar) [Occhipinti et al., 2013]. Therefore, the combination of geographic location (low, middle, or high latitudes), observational method and type of disturbance (gravity or acoustic wave) play an important role in both the generation and detection of these signals. In this paper, we will discuss the application of a particular methodology (virtual array beamforming) in Antarctica, where the orientation of the geomagnetic field allows generating and observing acoustic wave-induced TEC signals produced by seismic activity.

The TEC perturbations produced by seismic activity are called coseismic ionospheric disturbances (CID) [Calais and Minster, 1995; Heki and Ping, 2005; Astafyeva and Afraimovich, 2006; Astafyeva et al., 2009]. There are two types of CIDs: low-frequency acoustic waves triggered in the epicentral area by vertical coseismic offsets and acoustic waves induced by the vertical component of propagating Rayleigh waves [Rolland et al., 2011]. The propagation properties of these signals (e.g., apparent velocity and azimuth) are of great importance to

understand the physical mechanism that governs this phenomenon. Most of the publications that use GPS to study these signals obtain the apparent velocity using a time-distance diagram, a plot that shows the TEC perturbation amplitude as a function of time and distance from the source. The use of this diagram, however, depends on visual detection of the perturbation, and therefore, its signal-to-noise ratio (SNR) has to be high enough to allow the disturbance to be visually observed in the diagram as high and low TEC lineaments. The time-distance plot also does not provide azimuth information. While the first type of TEC wave can only be generated within approximately one fault length from the epicenter, the second type may be generated at teleseismic distances. Observations at teleseismic distances, or regions with noisy ionospheric environments, may result in signals with very low SNR (especially with low magnitude events), making use of a time-distance diagram challenging or even impossible.

To increase the SNR of the signal and estimate both apparent velocity and back azimuth (the direction to the source) we can use array beamforming, which is commonly used in seismology. For plane wave ionospheric disturbances, *Calais et al.* [2003] showed how to beamform observations obtained by a dense GPS network. This technique was developed for the analysis of traveling ionospheric disturbances rather than acoustic plane wave induced TEC signals, such as CIDs, although some authors have applied slant-stacking, a 1-D version of beamforming, to CIDs [*Afraimovich et al.*, 2001; *Astafyeva et al.*, 2009; *Dautermann et al.*, 2009]. A significant difference between the seismic and TEC GPS arrays is that the former provides measurements at fixed locations, those of the seismometers, while the latter provides measurements at the ionospheric piercing points (IPP), the moving intersections of the satellite-receiver LOS, and the peak electron density in the ionospheric *F* layer. The most basic GPS array is built from the IPPs between a set of GPS stations and a single satellite. We will refer to the array of IPPs where the TEC measurements are made as a virtual array because the observations are not obtained by physical sensors at the IPPs. Each GPS receiver records a TEC signal at the IPP that for a plane wave has a delay proportional to the apparent velocity of the signal and the position of the sensor along the raypath. Beamforming searches the delay space to find the set of delays producing the maximum energy of the stacked data, therefore amplifying the signal. This set of delays defines the plane wave apparent velocity and back azimuth.

Although GPS arrays have proven useful for observing TEC waves, the standard application does not take into account the following four effects. The first and second effects are related to coupling between the neutral atmospheric wave and the ionospheric plasma, and the geometrical relationship between the LOS and the propagation direction of the acoustic wave [*Georges and Hooke*, 1970]. These two effects alter the phase and amplitude of the TEC signals with respect to the inducing acoustic wave, i.e., the TEC signals are no longer plane waves and cannot be used in beamforming. The third effect is related to the average movement of the array, which can change the estimated apparent velocity and back azimuth, although in certain cases this effect may be ignored. Finally, deformation of the internal geometry of the array can result in an incorrect stacking.

To apply beamforming based on GPS TEC data, we will obtain an inverse transfer function using a model for GPS TEC observations to invert for the neutral acoustic wave that produced the TEC perturbation. Next, virtual array beamforming will be described and applied to the inverted neutral acoustic waves. Finally, we will apply virtual array beamforming to the inverted neutral acoustic waves during the passage of seismic waves from the Maule and Tohoku-Oki earthquakes from the Antarctic Network (ANET) component of the Polar Earth Observing Network project. The apparent velocities, back azimuths, and waveforms are found to agree with the hypothesis that they were produced by Rayleigh wave-induced acoustic waves from the earthquakes. The epicentral distances of ~7500 km and 12,500 km from the Maule and Tohoku-Oki earthquakes, respectively, make these, to our knowledge, the farthest observations of CIDs ever recorded with GPS.

2. A Model for GPS TEC Observations

Georges and Hooke [1970] developed a model (henceforth, the G&H model) coupling mono-frequency acoustic waves to the ionospheric plasma. This model quantifies the phase and amplitude of the induced GPS TEC measurements occurring in a plane-stratified *F* layer in the presence of a constant geomagnetic field, observed along the LOS to geostationary or moving satellites. We applied the G&H model at each IPP to account for the spatial variation of the geomagnetic field using the International Geomagnetic Reference Field (IGRF, see Data Sources section) to improve modeling of the acoustic wave-induced TEC signals. We

use this model with some further approximations to estimate the effect of Rayleigh waves on the ionosphere because our goal is to develop a beamforming technique rather than study the TEC response in detail. For a complete model of the effect of Rayleigh waves in the ionosphere, the reader should refer to *Rolland et al. [2011]* (using TEC observations) and *Artru et al. [2004]* (using Doppler sounding observations).

We simulate Rayleigh wave-induced acoustic wave packets in the neutral atmosphere by modulating a mono-frequency traveling wave with a moving exponential traveling taper, both traveling with the same speed:

$$u(\mathbf{r}, t) = A \exp[i(\omega t - \mathbf{k} \cdot \mathbf{r})] \exp\left[-(\omega t + \mathbf{k} \cdot \mathbf{r})^2 / \sigma\right] \quad (1)$$

where \mathbf{k} is the wave number and \mathbf{r} is the IPP LOS vector, A is the amplitude of the traveling wave packet, ω is the angular frequency of the traveling wave, and σ is a constant that controls the width of the exponential taper. This simplistic mono-frequency model is consistent with the G&H model, which requires a mono-frequency wave input to obtain the TEC response. Furthermore, the solid earth modes couple efficiently with the atmosphere at resonant frequencies of ~ 3.7 and ~ 4.4 mHz [*Lognonné et al., 1998, 2006; Artru et al., 2004; Rolland et al., 2011*]. This coupling acts as a narrow band-pass filter on the induced atmospheric wave, which then couples to the ionospheric plasma. To remove other TEC signals that do not match the resonant frequency of ~ 4.4 mHz, we will apply a narrow band-pass filter to the TEC times series. The filtering is also appropriate for use with beamforming and the G&H mono-frequency model.

Another simplification that we have imposed is that the transfer function between the solid earth and the atmosphere is equal to one, which means that we have not modeled the solid earth-atmosphere coupling. Equation (1) therefore can be used to model both the acoustic wave and the inducing solid earth Rayleigh wave, both of which have back azimuths that approximately point to the location of the epicenter. The vertical component of the Rayleigh wave will produce an acoustic wave with a takeoff inclination angle that can be estimated using simple wave propagation geometry. For a reasonable value of Rayleigh wave speed (~ 4 km/s) and sound speed at sea level (~ 0.33 km/s), the takeoff inclination angle is $\sim 5^\circ$. To provide the best estimate of the acoustic wave at the ionosphere we raytrace the acoustic wave from the ground surface to ionospheric altitudes before applying the G&H model. During this raytrace, we did not consider atmospheric dispersion, since this effect is small and usually ignored in propagation models for TEC perturbations, especially in low-energy events [*Dautermann et al., 2009*].

Garcés et al. [1998] presented a tau- p method for sound waves propagating in a stratified atmosphere under the influence of horizontal height-dependent winds. Using this 1-D raytrace, we estimate the propagation azimuth and incidence angle of the acoustic wave at ionospheric altitudes. The initial propagation azimuth at ground level is assumed to be that of the Rayleigh wave propagating from the epicenter. As the wave propagates upward, this initial azimuth will suffer from changes produced by horizontal winds. Atmospheric temperature and height-dependent winds were estimated using the NRL-MSISE model [*Picone et al., 2002*] and the Horizontal Wind Model 2007 (HWM07) [*Drob et al., 2008*]. In Antarctica, strong winds produce variations in azimuth and inclination of $\sim -40^\circ$ to 40° and $\sim 10^\circ$ to 17° , respectively. Previous implementations of similar ray tracing techniques have proven to be adequate to estimate the acoustic raypath [*Dautermann et al., 2009*].

Next, we couple the neutral wave with the ionospheric plasma to obtain the TEC response observed using GPS. For a LOS that crosses the whole ionospheric F layer, the observed change in ambient TEC induced by an acoustic plane wave is given by

$$C = \left[u e^{i(\omega t + \eta h_m)} \right] \left[\frac{1}{\omega \cos^2(\chi)} \right] \left[(\hat{\mathbf{k}} \cdot \hat{\mathbf{b}}) (\hat{\mathbf{r}} \times \hat{\mathbf{b}}) \times \hat{\mathbf{z}} \cdot \hat{\mathbf{k}} \right] \left[\int_{-\infty}^{\infty} n_{e0}(h_m + z') e^{i\eta z'} dz' \right] \quad (2)$$

where $\hat{\mathbf{b}}$, $\hat{\mathbf{r}}$, $\hat{\mathbf{z}}$, $\hat{\mathbf{k}}$ are the unit vectors for the geomagnetic field, LOS, the local vertical, and wave propagation directions; ω is the angular frequency; u is the amplitude of the neutral gas motions; \mathbf{k} is the wave number vector of the neutral gas wave (for a neutral acoustic wave, $\mathbf{U} = u\hat{\mathbf{k}}$); χ is the satellite zenith angle; $\eta = \frac{\mathbf{k} \cdot \mathbf{r}}{h_m}$, h_m is the altitude of the peak ionospheric electron density; \mathbf{r} is the position vector of the IPP, $z' = z - h_m$; and $n_{e0}(z)$ is the unperturbed electron density value as a function of altitude [*Georges and Hooke, 1970*]. It should be noted that we are only considering pressure waves, such as those observed in Rayleigh wave-induced acoustic waves. This can be justified by calculating the acoustic cutoff frequency, estimated using the atmospheric temperature values from the NRL-MSISE model. The estimated acoustic cutoff frequency

has a typical value of ~ 3.3 mHz [Artru *et al.*, 2004] up to an altitude of ~ 90 km, where it reaches a maximum value of ~ 3.9 mHz, below the narrow band-pass filter (4–7 mHz) applied to the TEC time series. To facilitate discussion of (2), we have broken it into four terms (in brackets): the traveling wave, satellite elevation, geometrical, and phase cancellation terms. A very detailed analysis and the derivation of this model can be found in Georges [1968], Hooke [1968], and Georges and Hooke [1970].

To use the virtual array beamforming technique, we need to obtain the transfer function between the neutral wave and the ionospheric plasma. Following Georges and Hooke [1970] and integrating the phase cancellation term in (2) for an α -Chapman profile, we obtain

$$PC = \frac{2^{-i\eta H}}{\sqrt{\pi}} \Gamma\left(\frac{1}{2} - i\eta H\right), \quad (3)$$

where PC denotes the phase cancellation term of an acoustic plane wave propagating with \mathbf{k} , Γ is the gamma function of complex argument, and H is the α -Chapman scale height (thickness of the ionosphere). Equation (3), which is complex valued, provides an estimate of the phase and amplitude of the TEC response at each IPP [Georges and Hooke, 1970]. The phase change of the TEC response with respect to the neutral acoustic wave, expressed by (3), will have the largest impact in beamforming and will be discussed later.

We will now briefly examine the geometrical term:

$$G = \left[(\hat{\mathbf{k}} \cdot \hat{\mathbf{b}}) (\hat{\mathbf{r}} \times \hat{\mathbf{b}}) \times \hat{\mathbf{z}} \cdot \mathbf{k} \right] \quad (4)$$

Amplitude changes of the TEC response do not have a large influence on beamforming, because they only produce a weighting effect on each trace, affecting the magnitude of the stacked signal. These terms, however, are important because they can produce a sign change in the TEC response, which masquerades as a 180° phase shift that would change constructive interference into destructive interference during beamforming. Since $\hat{\mathbf{b}}$ is near vertical at the geomagnetic poles and Rayleigh wave-induced acoustic waves propagate almost vertically, the $\hat{\mathbf{k}}$ and $\hat{\mathbf{b}}$ are subparallel in Antarctica and the $\hat{\mathbf{k}} \cdot \hat{\mathbf{b}}$ term should not produce sign changes in the TEC response. The $(\hat{\mathbf{r}} \times \hat{\mathbf{b}}) \times \hat{\mathbf{z}} \cdot \mathbf{k}$ term, however, is related to the relative orientation of the geomagnetic field and the observation direction (assuming a constant \mathbf{k}). If we consider the case of having constant \mathbf{k} and $\hat{\mathbf{b}}$, a change in direction of $\hat{\mathbf{r}}$ can generate a change in sign of the dot product with \mathbf{k} .

Finally, we have the satellite elevation term:

$$SE = \left[\frac{1}{\omega \cos^2(\chi)} \right] \quad (5)$$

which provides another amplitude change. This term expresses the sensitivity change of a GPS LOS to an acoustic wave-induced TEC signal, which varies with LOS zenith angle, χ , as $\cos^{-2}(\chi)$. This term has no influence in beamforming other than increasing the SNR of the acoustic wave-induced TEC signal. We will return to the influence of GPS orbit geometry and satellite elevation angle on the sensitivity to acoustic wave-induced TEC signals in Antarctica later.

Combining (3), (4), and (5), we obtain the equation of the G&H transfer function, which is independent of the shape of the mono-frequency acoustic wave:

$$T = \left[\frac{1}{\omega \cos^2(\chi)} \right] \left[(\hat{\mathbf{k}} \cdot \hat{\mathbf{b}}) (\hat{\mathbf{r}} \times \hat{\mathbf{b}}) \times \hat{\mathbf{z}} \cdot \mathbf{k} \right] \left[\frac{2^{-i\eta H}}{\sqrt{\pi}} \Gamma\left(\frac{1}{2} - i\eta H\right) \right]. \quad (6)$$

We analyzed the phase and amplitude effects of (6) using the acoustic wave model in (1) with the parameters of a synthetic acoustic wave produced by the Maule earthquake, two GPS stations located in Antarctica (COTE and MCM4), the International Reference Ionosphere (IRI) model [Bilitza *et al.*, 2014], and the IGRF model to obtain values for H , h_m , and $\hat{\mathbf{b}}$. Figures 1a and 1b show the phase and amplitude of the transfer function as a function of time, where we show that the phase of the TEC response can be different for the two IPP and that this difference changes as a function of time. A similar effect can be observed for the amplitude in Figure 1b, since the amplitude of the TEC response is different and also changes as a function of time.

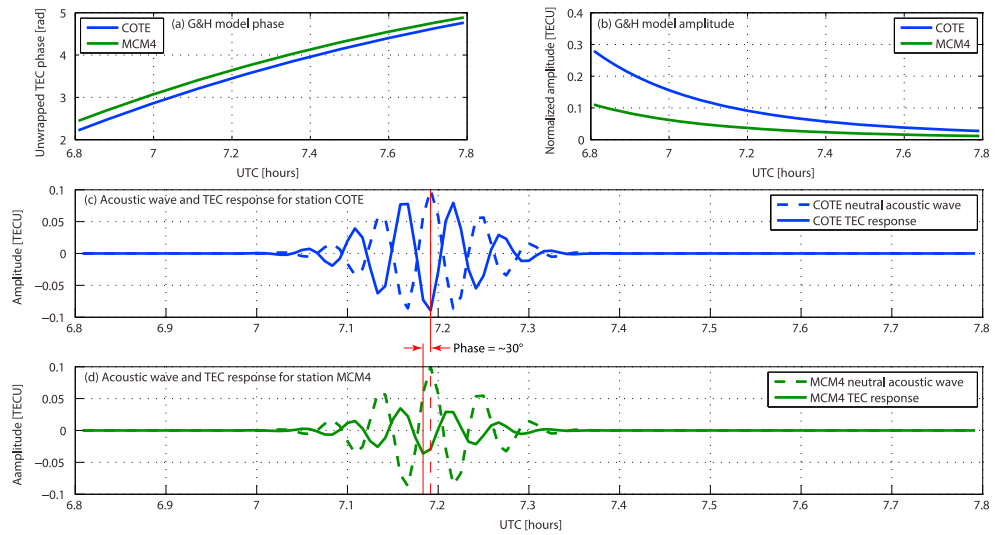


Figure 1. Synthetic TEC response to an acoustic wave using the G&H transfer function. (a) Phase of the TEC response as a function of time for GPS stations COTE and MCM4. (b) TEC amplitude response as a function of time. (c) Acoustic wave produced using a simple Rayleigh wave model (dashed line) and the corresponding TEC response (solid line) for station COTE. Vertical solid red line shows the maximum amplitudes of the TEC and acoustic wave signals that have a phase difference of $\sim 180^\circ$. (d) Same as Figure 1c, for station MCM4. Vertical solid red line shows the maximum amplitude of the TEC signal, while the dashed line shows the maximum amplitude of the acoustic wave signal with a phase difference of $\sim 150^\circ$. The phase difference between the TEC responses at COTE and MCM4 is $\sim 30^\circ$.

Figures 1c and 1d show a phase shift of $\sim 180^\circ$ in the TEC responses. The response for MCM4, however, differs from that of COTE by $\sim 30^\circ$. In addition to the time delay introduced by the distance between COTE and MCM4, the phase shift introduced by the G&H transfer function adds an additional phase shift, marked in Figure 1d by the difference between the vertical solid and dashed red lines. This synthetic test shows that for two locations relatively close to one another, the TEC response to an acoustic wave can have a significant time shift difference introduced by the phase cancellation term in (3). Since the phase of the wave-induced TEC signal changes nonuniformly across an array, we cannot beamform the raw TEC data because their phases do not correspond to those of a plane wave. In the following section we will describe how to invert for the plane acoustic wave that induced the TEC signal.

3. Recovery of the Neutral Acoustic Wave

The transfer function between the acoustic wave and the resulting induced TEC wave is complex, producing amplitude and phase changes in the TEC observation with respect to the acoustic wave. We will now develop the inverse transfer function to obtain the neutral acoustic wave from the TEC observations.

First, we will isolate the terms that only affect the phase of the transfer function: the phase cancellation (3) and geometrical (4) components. Normalizing (3) and considering only the sign of (4), we find the G&H forward transfer function phase contribution:

$$F = \text{sgn} \left(\left[(\hat{\mathbf{k}} \cdot \hat{\mathbf{b}}) (\hat{\mathbf{r}} \times \hat{\mathbf{b}}) \times \hat{\mathbf{z}} \cdot \mathbf{k} \right] \left[\frac{2^{-i\eta H} \Gamma(\frac{1}{2} - i\eta H)}{\sqrt{\pi}} \right] \right). \quad (7)$$

As η , H , \mathbf{k} , $\hat{\mathbf{b}}$, $\hat{\mathbf{r}}$ and $\hat{\mathbf{z}}$ are known, we can evaluate (7). To invert for the acoustic input wave therefore we divide the analytic signal (obtained using the Hilbert transform) of the TEC time series by (7) keeping only the real part. Note that because (7) is normalized, the input acoustic wave will have the same amplitude as the TEC signal.

Assuming a \mathbf{k} for (7), which corresponds to a wave produced by a “test” source, we can invert for the acoustic wave that induced the observed TEC signal. We then beamform these inverted signals, using the virtual beamform algorithm described later, to stack and amplify the acoustic plane wave and obtain an estimate

of its \mathbf{k} . If the beamformed \mathbf{k} agrees with the \mathbf{k} of the test source, and the synthetic TEC signal, obtained from forward modeling using (1) and (6), also agrees with the observed TEC time series, this provides a solid confirmation that the observed TEC signals were produced by the test source used to obtain the inverted acoustic waves.

In this work we have only applied the inverse transfer function using the test sources that correspond to those of the Maule and Tohoku-Oki earthquakes, because it is out of our scope to search for other TEC signals. Therefore, the acoustic plane wave of another TEC signal produced by a different source (ergo, with a different \mathbf{k}) is not correctly recovered. As a consequence, the beamform will not correctly stack signals with other than the test \mathbf{k} . This limitation is also related to the fact that performing an acoustic ray trace for each \mathbf{k} in the search space is very computationally expensive. If the effect of the winds can be ignored, applying the inverse transfer function for each \mathbf{k} is, more or less, trivial and the inverse transfer function can be applied for every \mathbf{k} in the search space allowing the beamform to find the acoustic plane wave that produces the maximum energy in the stack. In Antarctica the effect of the strong winds cannot be ignored, and therefore, one ray trace is needed for each \mathbf{k} if we want to allow the beamform to search for the signal without any a priori information. In this work, however, we are searching for a specific signal for which we know the propagation parameters that allow us to use a test source.

We should note that even for cases where we select an incorrect test source, the beamform will not detect a false signal if no acoustic plane wave is present in the time series. Furthermore, if a signal corresponding to a different source randomly stacks when applying an incorrect test source, the synthetic TEC time series will not agree with the GPS TEC measurements, and therefore, the test source can be discarded as the origin of the TEC disturbance. For the case of Rayleigh wave-induced signals, the detection of a signal can be further confirmed by comparing a seismogram waveform with the stacked acoustic wave signal.

4. Virtual Array Processing

We now present the virtual array technique and how it can be applied in a more general context, allowing array movement and deformation. A traveling wave at a fixed observation point located at \mathbf{r} can be represented by

$$u(t, \mathbf{r}) = f(t - \mathbf{p} \cdot \mathbf{r}), \quad (8)$$

where $u(t)$ is the observed signal at \mathbf{r} (e.g., a seismogram); $f(y)$ gives the shape of the wave as a function of the argument, $y = t - \mathbf{p} \cdot \mathbf{r}$; t is time; and \mathbf{p} is the slowness vector or ray parameter, defined as $\mathbf{p} = v^{-1}[\cos(\theta), \sin(\theta)]$, where v is the apparent velocity of the wave and θ is the horizontal azimuth of the traveling wave. For an array of sensors, each array element, i , will produce a time series:

$$u_i(t, \mathbf{r}_i) = f(t - \mathbf{p} \cdot \mathbf{r}_i). \quad (9)$$

As the ray parameter is a constant, it can be estimated by finding the time shifts, which are a function of \mathbf{r}_i and the ray parameter that align the $u_i(t, \mathbf{r}_i)$ such that they constructively interfere. This is accomplished by performing a grid search over the v, θ domain of the ray parameter (see *Rost and Thomas [2002]* for a complete review).

When observing TEC in the ionosphere using GPS, the array sensors are the IPPs. Because of the relative motion between the satellites and a point on the surface of the Earth, the position of the IPPs is a function of time. Taking this movement into account (9) becomes

$$u_i[t, \mathbf{r}_i(t)] = f[t - \mathbf{p} \cdot \mathbf{r}_i(t)]. \quad (10)$$

Since $\mathbf{r}_i(t)$ is now a function of time, this introduces potential rotation with respect to the geographic coordinate system, translation, and deformation of the array.

To apply beamforming to a moving array we first need to address some geometrical considerations related to the rotation of the array with respect to the geographic coordinate system that are especially important near the geographic poles. In standard beamforming, where the sensors are fixed, a local coordinate system is used to specify the coordinates \mathbf{r}_i . This coordinate system is constant during the time of the analysis, and typically aligned with true north to obtain the orientation of the traveling plane wave, since \mathbf{p} is a function of the horizontal azimuth, θ , in the coordinate system. In general, for the case of a moving array, both the location of

the array and the direction of true north will change as a function of time. This change in the direction of true north is particularly strong at high latitudes, where small changes in position result in large rotations in a local coordinate system aligned with true north. In this study, the Rayleigh wave-induced signals are ten to 20 min in duration, and we are far enough from the geographic pole that the change in orientation during this time period, due to the rotation with respect to true north of the array, is small and can be ignored.

We will now examine the effects of the translation and deformation of an array on beamforming. The deformation of the array will produce a changing internal array geometry that, due to the dependence on $\mathbf{r}_i(t)$, is equivalent to having a different array at each time sample. This can be illustrated by considering a series of snapshots of the wavefield centered on the array and oriented with respect to true north, with the position of the array sensors marked in each snapshot. A Doppler shift in the time series at each sensor will be generated by the movement of the sensors with respect to the wavefield. By considering each time sample as an independent array, however, we will see that we do not have to explicitly correct for this Doppler shift.

To beamform, each time series is shifted to bring it to the origin of the instantaneous coordinate system, which can be a particular array sensor. Because each snapshot (time sample) is considered to form an independent array, it will have its own time shift given by

$$\tau_i[\mathbf{p}, \mathbf{r}_i(t)] = \mathbf{p} \cdot \mathbf{r}_i(t) = p_x x_i(t) + p_y y_i(t). \quad (11)$$

where $x_i(t)$, $y_i(t)$ are in the instantaneous local Cartesian coordinate system. The standard beamform time shift $\tau_i[\mathbf{p}, \mathbf{r}_i(t)]$ applied to the instantaneous array removes the requirement to explicitly correct for the Doppler shift due to the array deformation. We should note that because the components of both \mathbf{p} (recalling that \mathbf{p} is a function of the horizontal azimuth) and $\mathbf{r}_i(t)$ are a function of an instantaneous local coordinate system, the time shift to bring each sample to the origin position, $\tau_i[\mathbf{p}, \mathbf{r}_i(t)]$, is not constant and the shifting operation for beamform stacking must therefore be performed in the time domain.

Let the origin of the instantaneous local coordinate systems be assigned to one of the array sensors, hereafter the “reference sensor” (RS). By (11) no time shifts will be applied to its time series. While we do not have to explicitly consider the Doppler shift from the array deformation, the Doppler shift generated by the movement of the RS itself still has to be considered. This Doppler shift will generate a difference in the estimated ray parameter and back azimuth. If the velocity of the array is much, much, less than the apparent velocity of the wave, the error introduced into the back azimuth and apparent velocity estimate will be small and the apparent velocity found by beamforming will be the sum of the wave apparent velocity and the velocity of the array.

Figure 2 shows a summary of these effects and how observations at different latitudes can produce different array deformations. Figures 2a and 2b show two virtual arrays around the time of the Maule earthquake, one at midlatitudes from the Maule area of South America during a 4 h time window (Figure 2a) and the other at high latitudes in Antarctica during a two and a half hour time window (Figure 2b). The blue traces show the displacement time series of each IPP in their local coordinate systems. As can be clearly seen, the deformation of the high latitude array is significantly larger than that at midlatitude. This difference is due to the GPS satellite orbit geometry. For the midlatitude array, where satellites can be found at high elevation angles and the deformation is minimal, standard beamforming works as in *Calais et al.* [2003]. For high latitude arrays, however, the satellite elevations are much lower, the IPPs move much faster than at midlatitude, significantly deforming the array and requiring the procedure described here. We should note that basing an array on a low elevation satellite at midlatitudes will also result in a similarly, rapidly deforming array.

In Figure 2c we show the time series of a traveling sine wave to illustrate the Doppler shift produced by the deformation of the array for two IPPs (COTE and ROB4) of the high latitude array. Taking a smaller time window (between ~8.45 and ~8.55 UTC), we plot the unshifted time series in Figure 2d showing the individual, simultaneous, samples. We then time-shift each sample of ROB4 using the procedure above to align it with the RS, COTE. We now observe that in the time-shifted series of ROB4, the sample rate is nonuniform and the sample times are different from those of COTE. We therefore have to resample the time series of ROB4 before stacking.

Now we have time series representing a plane wave (we use the inverted acoustic wave signals obtained from the TEC observations, not the raw TEC data) crossing a standard array. This more general method, that allows a large deformation of the array, can be applied to acoustic wave signals inverted from the TEC time series to recover low SNR TEC signatures in noisy ionospheric environments such as Antarctica [*Hunsucker and Hargreaves, 2002*].

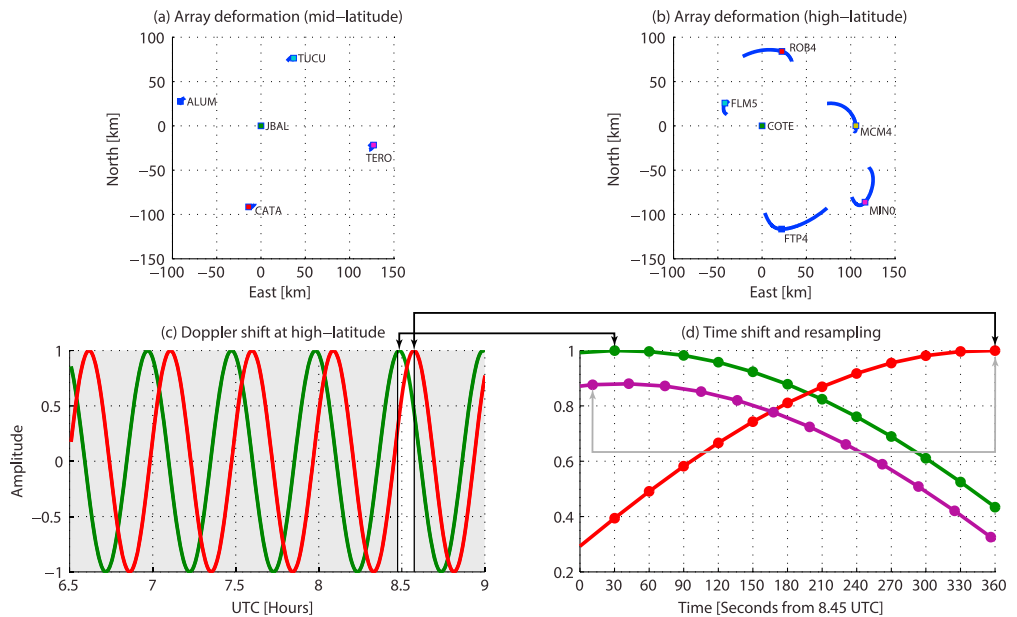


Figure 2. Comparison of deformation as a function of time for a virtual array over (a) 4 h at midlatitudes and (b) two and a half hours at high latitudes showing deformation is insignificant for the midlatitude array but very large for the high latitude array. (c) During the high latitude time window, we show a traveling sine wave with a back azimuth of 270° recorded by COTE (the RS, green) and ROB4 (red). The Doppler shift observed in the time series due to the deformation of the high latitude array is removed by the time shift based on the instantaneous array geometry during beamforming. (d) We show the unshifted traveling sine waves between ~ 8.45 and ~ 8.55 UTC (white section of the plot in Figure 2c). Dark arrows connecting Figures 2c and 2d show the correspondence between time samples of each time series. The time samples of the red and green traces match (solid circles). We apply the variable beamforming time shifts to align the time series of ROB4 (purple) with COTE (green). The light arrow shows the correspondence between the unshifted and beamform shifted position of a time sample. The time samples of the beamform shifted ROB4 time series are no longer coincident with those of COTE (green), and therefore, resampling is necessary before stacking. We applied a small vertical offset to the amplitude component of ROB4 to better visualize both time series.

We tested the virtual array beamform with synthetic data at an eight element array to show that it can successfully estimate apparent velocity and back azimuth of plane wave signals on an array that is experiencing large deformations, as happens in high latitude locations. We used the simple Rayleigh wave model in (1) propagating with a phase velocity of 4.2 km/s and a back azimuth at the array of $\sim 131^\circ$. The estimated apparent velocity and back azimuth was $\sim 4.5 \text{ km/s}$ and $\sim 135^\circ$, respectively, which is in very good agreement with the input data (Figures 3a and 3b). We also note that the proposed simplistic Rayleigh wave model is a good approximation for a narrow band-passed Rayleigh wave signal, as shown by the agreement between the stacked synthetics in Figure 3c and the band-passed (4 to 7 mHz) vertical component of the seismogram recorded at Wright Valley (VNDA), Antarctica, during the passage of seismic waves from the Maule earthquake.

Before describing the conditions that allow observing teleseismic Rayleigh wave-induced TEC signals in Antarctica, we will review the relation between the apparent velocity obtained by beamforming on a virtual array and the Rayleigh wave phase velocity. Figure 4a presents a simple diagram showing the components of GPS ionospheric observations. When an earthquake occurs, an N-shaped acoustic wave from the coseismic vertical component (first type of CID, see Introduction) is induced in the near-field atmosphere. In the middle to far field, the Rayleigh wave induces an acoustic wave that produces TEC perturbations after coupling with the ionospheric plasma.

Figure 4b shows that in 1-D, Rayleigh waves can be modeled as a traveling point source. The traveling point source releases energy into the atmosphere that travels almost vertically with the speed of sound. In this example, we have assumed a windless, homogeneous atmosphere to simplify our diagram. When the wave reaches each IPP of the virtual array (after coupling with the ionospheric plasma), the delay between each arrival is that of the horizontal speed or apparent velocity of the wave. The ray parameter determined by

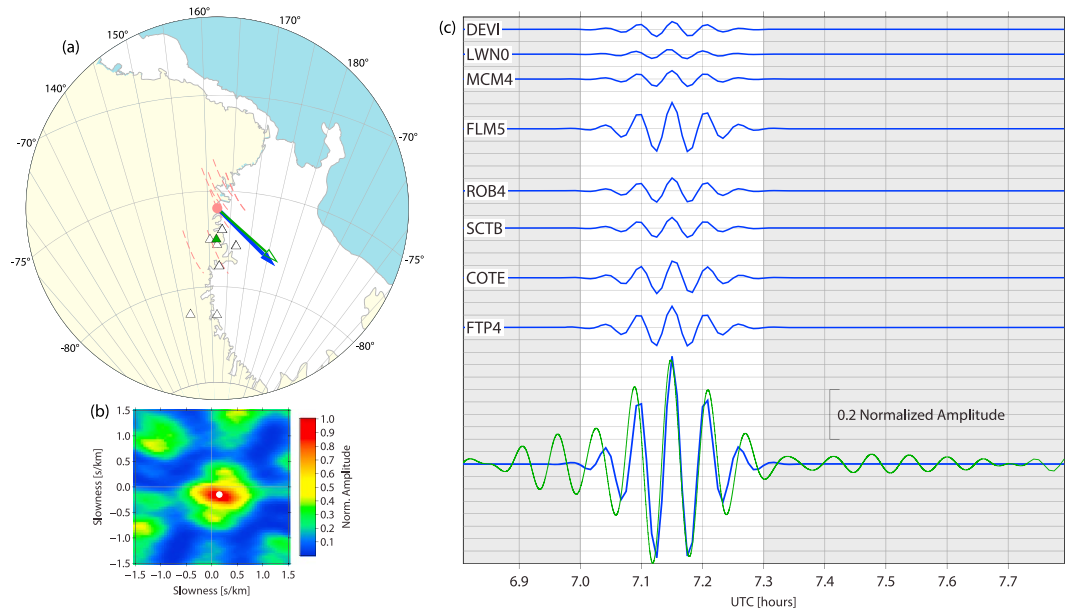


Figure 3. Results for virtual array beamform of synthetic acoustic waves, not coupled to the ionospheric plasma, produced by the Maule earthquake. This represents the input signal to the ionosphere. (a) Map showing the beamform estimated back azimuth (blue arrow, $\sim 135^\circ$), the great circle back azimuth (green arrow, $\sim 131^\circ$), and the virtual array IPP's paths (red dashed lines). (b) Beamform plot showing the maximum energy stack with a slowness of ~ 0.22 s/km (speed = ~ 4.5 km/s), in agreement with the synthetic Rayleigh wave speed of 4.2 km/s (c) Top: time-shifted, acoustic wave synthetics at each GPS station (blue traces). Bottom: acoustic wave stack result (blue trace), and time-shifted seismogram (green trace) recorded at seismic station Vnda (green triangle), to show the agreement between our synthetic Rayleigh wave model and the seismic data.

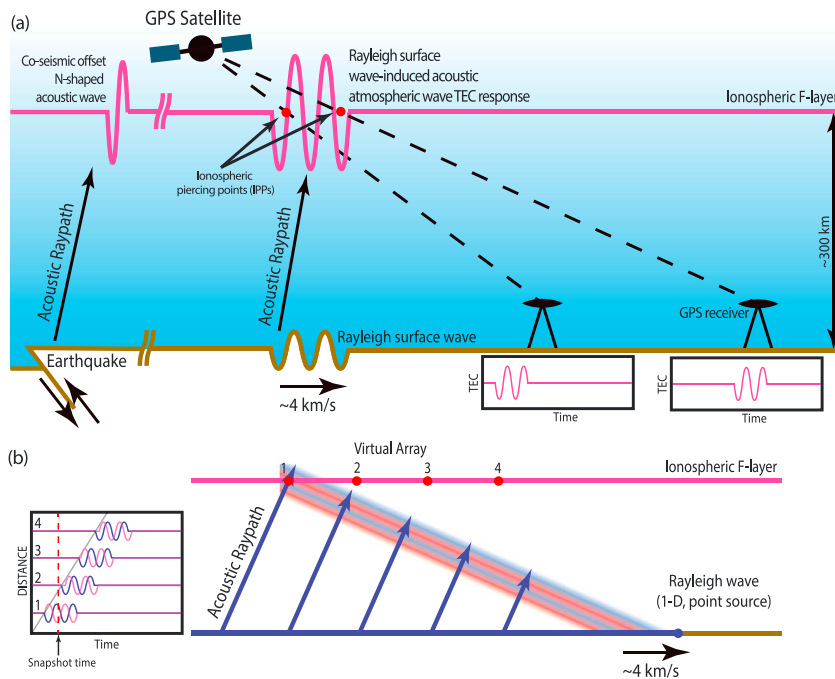


Figure 4. (a): Diagram of the ionospheric piercing point (IPP) geometry and acoustic raypath. Two GPS stations are shown with their TEC signal plots. (b) Relation between virtual array beamformed apparent velocity and Rayleigh wave phase velocity. The diagram does not illustrate the temporal deformation of the array and assumes a windless and constant sound speed atmosphere. The left pane shows the acoustic wave amplitude as a function of time and distance (blue lines) and the TEC response (magenta lines). Note that the phase of the TEC response is different at each IPP to show the effect of the coupling between the neutral wave and the ionospheric plasma.

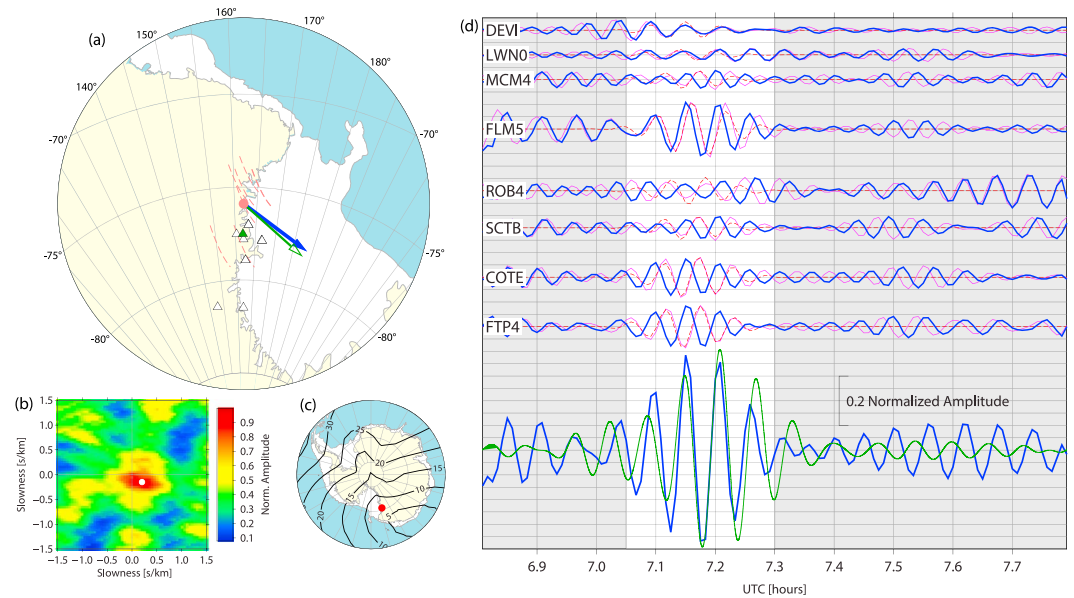


Figure 5. Results for virtual array beamform of CIDs produced by the Maule earthquake. (a) Location map. White triangles show the GPS stations; green triangle shows the VNSA seismic station. Red dashed lines show IPP paths. Red filled circle shows the array center location. Arrows show the back azimuths; to epicenter—green $\sim 135^\circ$, estimated using beamforming—blue $\sim 126^\circ$. (b) White circle shows the beamform stacking slowness (speed, ~ 4 km/s). (c) Contour map showing the inclination of the geomagnetic field lines and the position of the virtual array, red filled circle ($\sim 7.5^\circ$). (d) Top: TEC observations—magenta, TEC synthetics—dashed red, using the Rayleigh wave back azimuth and speed (4 km/s), the atmospheric temperature (MSIS), wind (HWM07), and geomagnetic (IGRF) and G&H models, time-shifted acoustic waves inverted from TEC observations using (7)—blue; bottom: stacked TEC signal using the beamform virtual array—blue; vertical component of seismogram recorded at VNSA station—green. The seismic trace is vertically scaled to match the acoustic wave amplitude and shifted in time using the atmospheric ray tracing.

the beamform of the induced acoustic wave is equal to the ray parameter of the inducing Rayleigh wave, which is the inverse of its phase velocity. Although the ray parameter of an ideal wavefront is constant throughout the atmospheric propagation, localized winds and temperature variations may distort the wavefront and change the arrival time of individual rays to each IPP. This deformation of the wavefront due to winds, however, can be removed by raytracing the acoustic wave.

5. Observation of Teleseismic Rayleigh Waves in Antarctica

TEC signatures produced by Rayleigh wave-induced acoustic waves have previously been observed as far as ~ 3000 km from earthquakes [Heki and Ping, 2005; Astafyeva and Afraimovich, 2006; Astafyeva et al., 2009; Galvan et al., 2012]. Beyond this distance, attenuation of the ionospheric TEC response to Rayleigh waves appears to fall-off, either because of the attenuation of the Rayleigh waves or because conditions to observe ionospheric wave-induced perturbations (geomagnetic field inclination, LOS orientation, etc.) are not met beyond some distance.

The elevation angle of GPS satellites due to the GPS orbit inclination is of particular importance in Antarctica when observing Rayleigh wave-induced TEC signals. From (6) we find that the observation of the wave-induced change in TEC varies with LOS zenith angle, χ , as $\cos^{-2}(\chi)$. This term becomes large for low satellite elevation (large χ), increasing the sensitivity to TEC waves as the LOS elevation decreases. A review of observations of ionospheric perturbations as a function of satellite elevation done by Rolland et al. [2011] also concluded that low satellite elevations favor the observation of ionospheric Rayleigh wave-induced perturbations.

Polar regions are therefore optimal for observing Rayleigh wave CIDs in the ionosphere, because of the low elevation of GPS satellites and the efficient coupling with the ionospheric plasma produced by acoustic waves that are subparallel to the geomagnetic field. This is supported by the observations reported here

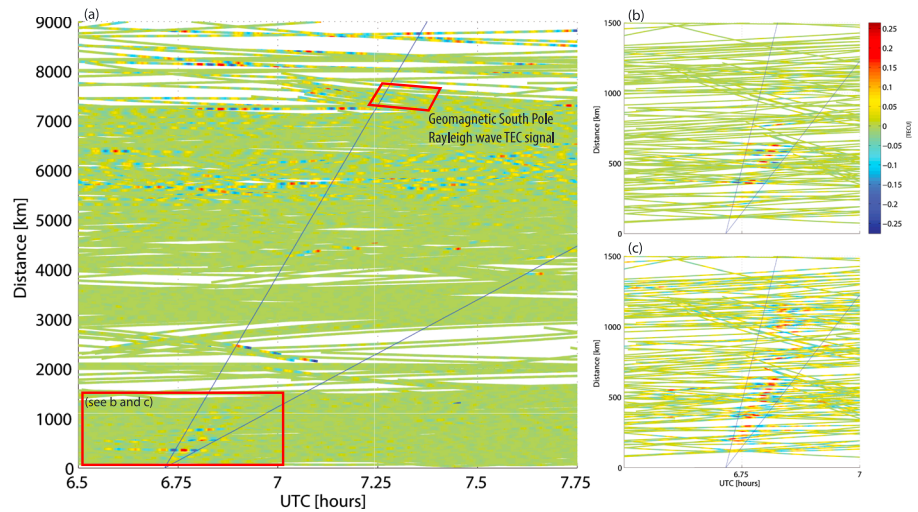


Figure 6. (a): Traditional time-distance diagram of TEC for GPS stations between the epicentral region of the Maule earthquake and the McMurdo region in Antarctica. The Rayleigh wave-induced TEC signal from the Maule earthquake, processed in the beamform analysis, can be observed in Antarctica in the distance range 7200 to 7800 km (top red polygon). Due to the low number of GPS stations in southern South America and Antarctica, all GPS stations-satellite pairs are shown in the time-distance diagram. The steep blue line shows the Rayleigh wave propagation from the epicentral area (slope = 4 km/s). The shallower blue line shows the N-shaped acoustic wave (slope = 1 km/s). We applied a delay of ~10 min to the origin times of the blue lines to account for the travel time from the ground to the ionosphere. The earthquake origin time is ~6.5 UTC. To enhance visibility of the far field signals, we only plotted TEC traces with both high SNR and absolute amplitudes $< \sim 0.25$ total electron content unit (TECU, 1 TECU = 10^{16} el m⁻²) in which the Rayleigh wave-induced TEC signals are observable. The data in the lower red box are shown in Figures 6b and 6c. (b): Zoom in showing the acoustic wave-induced TEC signals in the near field. Blue lines as in Figure 6a. Because only TEC traces with amplitudes $< \sim 0.25$ TECU were plotted, the signals are less visible beyond ~800 km. (c) View of the TEC signals shown in Figure 6b, enhanced using an automatic gain control algorithm. This plot shows absolute amplitude differences from -1 (blue) to 1 (red).

of Rayleigh wave-induced TEC perturbations produced by very distant seismic sources in the vicinity of the Geomagnetic South Pole.

6. Virtual Beamforming the Maule Earthquake TEC Signals in Antarctica

We performed virtual array beamforming on band-passed (4 to 7 mHz, or 2.38 to 4.16 min period) acoustic waves, inverted from the TEC time series using the G&H inverse transfer function (7), for a wave number vector corresponding to Rayleigh waves of the Maule earthquake, for a set of ANET stations in the vicinity of McMurdo (DEVI, LWN0, MCM4, FLM5, ROB4, SCTB, FTP4, and COTE), using satellite PRN02 on the day of the M_w 8.8 Maule earthquake (location 35.909°S, 72.733°W, depth 35 km on 27/02/2010 at 06:34:14 UTC). Although the SNR of the TEC signals is much lower than that of signals typically observed around epicentral areas [Calais and Minster, 1995; Astafyeva and Afraimovich, 2006; Astafyeva et al., 2009; Galvan et al., 2012], the beamform clearly detected the signal at the array, even though it is difficult to identify the signal in each individual time series.

Figures 5a and 5b show the map and beamform response, respectively, of a virtual array located in a region where the geomagnetic field lines are almost vertical (inclination of ~7.5°) as shown by Figure 5c. We estimated an apparent velocity of ~4 km/s (slowness of 0.25 s/km) and a back azimuth of ~126° that is in excellent agreement with the arrival of Rayleigh waves produced by the Maule earthquake. The virtual array response plot (Figure 5b) is also in good agreement with the synthetic test in Figure 3b.

Figure 5d shows the synthetic TEC traces obtained using the G&H model and the observed TEC signals for each IPP. We verify that the synthetic TEC time series, obtained using the Rayleigh wave function described by (1), are in good agreement with the TEC measurements. To obtain a better fit between the synthetics and TEC measurements, we estimated the ionospheric scale height from the IRI model allowing a small variation of less than 5% until the residual between model and data was minimized. We also show the time shifted, acoustic wave signals inverted using the inverse transfer function. The beamform stacked inverted acoustic

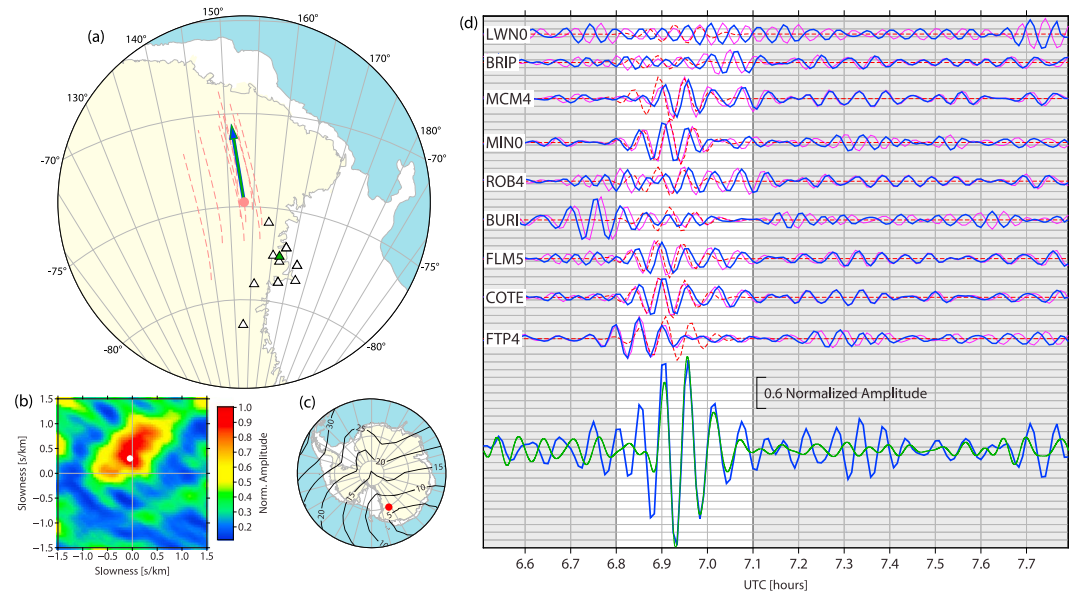


Figure 7. Results for virtual array beamform of CIDs produced by the Tohoku-Oki earthquake. Symbols as in Figure 5. (a) Location map. Back azimuths; to epicenter—green $\sim 350^\circ$, estimated using beamforming—blue $\sim 350^\circ$. (b) Beamform stacking slowness (speed, ~ 3.5 km/s). (c) inclination of the geomagnetic field lines ($\sim 6^\circ$). (d) Same as in Figure 5.

wave at the bottom of Figure 5d is in very good agreement with the vertical component of the seismogram recorded at VNDA, ~ 180 km from the center of the array, delayed by the calculated travel time from the ground to ionospheric altitudes. To better compare the agreement of the seismogram and the estimated acoustic wave signature obtained from TEC observations, we applied a small time offset necessary to better align these two traces, since the raytracing provides an arrival time that is accurate only within a few minutes. The synthetic TEC and the Rayleigh wave seismogram were scaled to match the TEC data and the amplitude of the stacked acoustic wave, respectively, because we have not modeled the coupling between the solid earth and the atmosphere, necessary to obtain the correct amplitudes.

The proximity of the Antarctic region to the epicentral area of the Maule earthquake allowed us to compare our results with those obtained by the traditional time-distance diagram. Figure 6a shows that the Rayleigh wave-induced ionospheric signal can also be identified from this diagram. This plot was generated using only TEC traces with high SNR, on which the Rayleigh wave-induced TEC signal is observable. Some induced signals in the near field can also be observed at ~ 600 km from the epicentral area (lower red box). These near-field TEC signals are also shown in Figures 6b and 6c. While low SNR signals are visible in the time-distance plots, the information that can be obtained from them is less than that obtained from the virtual array. We examined other ANET virtual arrays that are farther away from the geomagnetic pole, but the presence of Rayleigh wave-induced TEC signals was less certain. We suggest that this can be explained by a geomagnetic field inclination $> 10^\circ$ at the location of the arrays, which significantly reduces the coupling between the acoustic wave and the ionospheric plasma.

7. Virtual Beamforming the Tohoku-Oki Earthquake TEC Signals in Antarctica

We performed the same procedure with TEC observations using satellite PRN25 for the arrival time window of Rayleigh waves from the M_w 9.0 Tohoku-Oki earthquake, (location 38.297°N , 142.372°E , depth 30 km on 11/03/2011 at 05:45:24 UTC). Figures 7a and 7b show results similar to those from the Maule earthquake.

For the Tohoku-Oki earthquake, we have estimated a back azimuth of $\sim 350^\circ$, equal to the great circle back azimuth, and an apparent velocity of ~ 3.5 km/s (slowness of ~ 0.28 s/km). Although we assumed a Rayleigh wave phase velocity of ~ 4 km/s, our beamformed apparent velocity is within the observed Rayleigh wave velocity range found in previous studies [e.g., *Artru et al., 2001; Rolland et al., 2011*]. We also note that the location of both virtual arrays (Maule and Tohoku-Oki) is close together, as shown by Figure 7c, which suggests that a geomagnetic field inclination of less than $\sim 10^\circ$ favors the observation of this phenomenon.

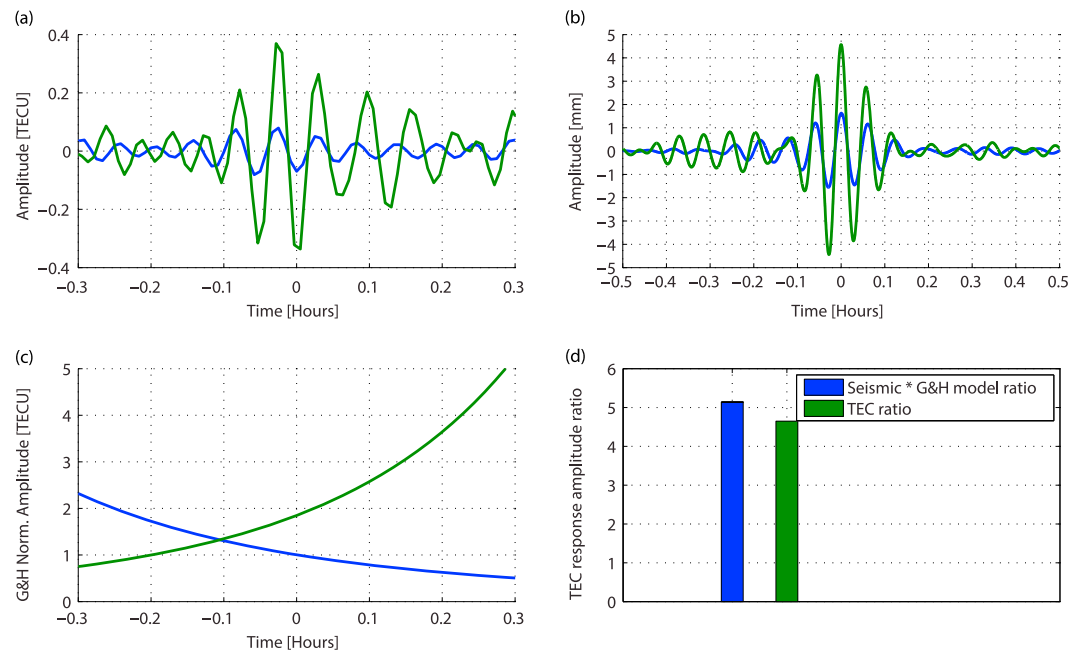


Figure 8. Amplitude comparison of the TEC response of the Maule and Tohoku-Oki earthquakes for two IPPs for the GPS station COTE. (a) TEC signals of the Maule (blue) and the Tohoku-Oki earthquakes (green). Time shifts were applied to place the Rayleigh wave-induced TEC signal at ~ 0 h. The peak to peak TEC amplitude of the Tohoku-Oki earthquake is 4.6 times larger than that of Maule. (b) Amplitude comparison of the band-passed and time shifted Rayleigh wave vertical component at seismic station VNDA for the Maule (blue) and the Tohoku-Oki (green) earthquakes. The peak to peak seismic amplitude shows that the Rayleigh wave from Tohoku-Oki is 3 times larger than that of Maule. (c): Transfer function amplitude scaled to the response of the Maule earthquake, which shows that the TEC response for the Tohoku-Oki earthquake is ~ 1.8 times larger than that for Maule. (d) Estimated response ratio using the seismic amplitude ratio times the transfer function ratio, which yields 5.1.

On Figure 7b, we note a “smeared” beamform response plot, which suggests the existence of a second TEC signal occurring within the time window of the TEC time series used for beamforming. Assuming the presence of a second TEC signal in the ionosphere, applying the inverse transfer function using the Tohoku-Oki test source could result in partial constructive interference. Secondary signals can be observed in the time series for stations BURI, FTP4, and LWN0 in Figure 7d, where wave packets outside the Rayleigh wave time window (gray section of the plot) can be seen. Nevertheless, coherent stacking among the nine elements of the virtual array beamform allowed us to distinguish the Rayleigh wave-induced acoustic wave from other signals and noise.

We also compared the amplitudes of the TEC response for Tohoku-Oki and Maule using the raw TEC data of GPS station COTE. We note that the amplitude at COTE of the Tohoku-Oki signal is about 4.6 times larger than that for Maule (Figure 8a), while the seismic displacement amplitude ratio is only a factor of three (Figure 8b). Assuming that the ratio of the acoustic wave is linearly proportional to the vertical amplitude of the Rayleigh waves, and multiplying this ratio by the TEC response ratio obtained from the G&H model (Figure 8c), we estimated a TEC ratio of ~ 5.1 (Figure 8d), which is roughly in agreement with the observed TEC ratio.

8. Conclusion

We have introduced a new approach, virtual array beamforming, for analyzing ionospheric TEC waves. This method allowed us to estimate the speed and back azimuth of seismically induced acoustic waves at the virtual array by amplifying the signals through coherent stacking. To recover the Rayleigh wave-induced acoustic waves from TEC observations, we used an inverse transfer function obtained from the G&H model. Our results strongly argue that the signals we observed in the ionosphere around the Geomagnetic South Pole were produced by the Maule and the Tohoku-Oki earthquakes.

We propose that the detection of CIDs in the region of the Geomagnetic South Pole is enhanced by two effects, the increase in sensitivity with lowering of the GPS LOS elevation, and the enhanced generation of

CIDs due the subparallel alignment of the geomagnetic field lines near the geomagnetic poles with the propagation direction of the acoustic wave. Although a high level of noise in the Antarctic ionosphere poses some difficulties for observing low SNR signals, by using virtual array beamforming we have observed Rayleigh wave-induced acoustic waves from events that are ~7500 km and ~12,500 km distant. To our knowledge, this is the farthest observation of this phenomenon using GPS technology.

The amplitude of the TEC response for Tohoku-Oki is about 4.6 times larger than that for Maule. Although we cannot perform a direct comparison of the ionospheric response of each earthquake without the appropriate solid earth-atmosphere coupling, as in *Rolland et al.* [2011], we approximate the TEC ratio by assuming that the ratio of the acoustic waves is linearly proportional to the vertical amplitude of the Rayleigh waves. Multiplying this ratio by the TEC response ratio obtained from the G&H model, we estimated a TEC ratio of ~5.1, which is roughly in agreement with the observed TEC ratio.

Evidence supporting teleseismic Rayleigh wave-induced acoustic wave observations at very large distances can be found in *Occhipinti et al.* [2010], who showed that the R2 signal produced by the 2005 (M_w 8.6) Sumatra earthquake could be detected in the ionosphere using an over-the-horizon radar and Doppler sounder observations. Their findings suggest that if a lower magnitude earthquake R2 Rayleigh wave induces a TEC signal, R1 of the Maule and Tohoku-Oki earthquakes will also induce a TEC signal at large distances from the epicenter. Because of the appropriate observational conditions, these signals can be recorded using GPS in Antarctica.

Another important factor for observing seismogenic TEC signals is the magnitude of the earthquake producing them. We also analyzed data from the M_w 8.2 Pisagua earthquake (location at 19.642°S, 70.817°W depth of 20.1 km on 01/04/2014 at 23:46:47 UTC). Although our results suggest the presence of Rayleigh wave-induced TEC signals near the Geomagnetic South Pole, the beamformed signal has a very low SNR that reduces our confidence in the results. However, this result and results from *Occhipinti et al.* [2010] suggest that earthquakes smaller than M_w 8.8 will generate signals near the Geomagnetic Poles that may be visible with GPS. Further modeling and the inclusion of solid earth-atmosphere coupling will help to better understand this observed polar phenomenon.

Data Sources

This material is based on data services provided by the UNAVCO Facility with support from the National Science Foundation (NSF) and National Aeronautics and Space Administration under NSF Cooperative Agreement EAR-0735156.

<http://www.unavco.org/>

Data for the Maule earthquake used to produce the time-distance diagram were obtained from the *Red Argentina de Monitoreo Satelital Continuo*, Instituto Geográfico Nacional, Argentina.

<http://www.ign.gob.ar/NuestrasActividades/Geodesia/Ramsac>

The International Geomagnetic Reference Field (IGRF) was obtained from the International Association of Geomagnetism and Aeronomy, Working Group V-MOD. doi:10.1111/j.1365-246X.2010.04804.x

An empirical model of the Earth's horizontal wind fields: HWM07 was downloaded from <http://nssdcftp.gsfc.nasa.gov/models/atmospheric/hwm07/>

The NRL-MSISE-00 Empirical Model of the Atmosphere was downloaded from: <ftp://hanna.ccmc.gsfc.nasa.gov/pub/modelweb/>

The International Reference Ionosphere 2012 was downloaded from: <http://iri.gsfc.nasa.gov/>. doi:10.1051/swsc/2014004

References

- Afraimovich, E. L., E. A. Kosogorov, N. P. Perevalova, and A. V. Plotnikov (2001), The use of GPS arrays in detecting shock-acoustic waves generated during rocket launchings, *J. Atmos. Sol. Terr. Phys.*, *63*(18), 1941–1957.
- Artru, J., P. Lognonné, and E. Blanc (2001), Normal modes modelling of post-seismic ionospheric oscillations, *Geophys. Res. Lett.*, *28*(4), 697–700, doi:10.1029/2000GL000085.
- Artru, J., T. Farges, and P. Lognonné (2004), Acoustic waves generated from seismic surface waves: Propagation properties determined from Doppler sounding observations and normal-mode modelling: Propagation of seismic acoustic waves, *Geophys. J. Int.*, *158*(3), 1067–1077, doi:10.1111/j.1365-246X.2004.02377.x.

Acknowledgments

This work was supported by National Science Foundation POLENET grants PLR0632339, PLR1247518 and PLR0948103 (Gómez and Smalley), ANT-0632322 and PLR-1249631 (Wilson, Bevis, Konfal, Willis and Caccamise), and ANT-06332330 and PLR-1249513 (Dalziel) and the Center for Earthquake Research and Information, The University of Memphis (Langston). The authors would like to thank Giovanni Occhipinti and an anonymous reviewer for their insightful comments and suggestions that have contributed to improve this paper.

- Artru, J., V. Ducic, H. Kanamori, P. Lognonné, and M. Murakami (2005), Ionospheric detection of gravity waves induced by tsunamis, *Geophys. J. Int.*, *160*(3), 840–848, doi:10.1111/j.1365-246X.2005.02552.x.
- Astafeyeva, E., K. Heki, V. Kiryushkin, E. Afraimovich, and S. Shalimov (2009), Two-mode long-distance propagation of coseismic ionosphere disturbances, *J. Geophys. Res.*, *114*, A10307, doi:10.1029/2008JA013853.
- Astafeyeva, E. I., and E. L. Afraimovich (2006), Long-distance traveling ionospheric disturbances caused by the great Sumatra-Andaman earthquake on 26 December 2004, *Earth Planets Space*, *58*(8), 1025–1031.
- Bilitza, D., D. Altadill, Y. Zhang, C. Mertens, V. Truhlik, P. Richards, L.-A. McKinnell, and B. Reinisch (2014), The International Reference Ionosphere 2012 – A model of international collaboration, *J. Space Weather Space Clim.*, *4*, 1–12, doi:10.1051/swsc/2014004.
- Calais, E., and J. B. Minster (1995), GPS detection of ionospheric perturbations following the January 17, 1994, Northridge earthquake, *Geophys. Res. Lett.*, *22*(9), 1045–1048, doi:10.1029/95GL00168.
- Calais, E., and J. B. Minster (1998), GPS, earthquakes, the ionosphere, and the Space Shuttle, *Phys. Earth Planet. Inter.*, *105*(3), 167–181.
- Calais, E., J. S. Haase, and J. B. Minster (2003), Detection of ionospheric perturbations using a dense GPS array in Southern California, *Geophys. Res. Lett.*, *30*(12), 1628, doi:10.1029/2003GL017708.
- Dautermann, T., E. Calais, and G. S. Mattioli (2009), Global Positioning System detection and energy estimation of the ionospheric wave caused by the 13 July 2003 explosion of the Soufrière Hills Volcano, Montserrat, *J. Geophys. Res.*, *114*, B02202, doi:10.1029/2008JB005722.
- Drob, D. P., et al. (2008), An empirical model of the Earth's horizontal wind fields: HWM07, *J. Geophys. Res.*, *113*, A12304, doi:10.1029/2008JA013668.
- Fitzgerald, T. J. (1997), Observations of total electron content perturbations on GPS signals caused by a ground level explosion, *J. Atmos. Sol. Terr. Phys.*, *59*(7), 829–834.
- Galvan, D. A., A. Komjathy, M. P. Hickey, P. Stephens, J. Snively, Y. Tony Song, M. D. Butala, and A. J. Mannucci (2012), Ionospheric signatures of Tohoku-Oki tsunami of March 11, 2011: Model comparisons near the epicenter, *Radio Sci.*, *47*, RS4003, doi:10.1029/2012RS005023.
- Garcés, M. A., R. A. Hansen, and K. G. Lindquist (1998), Traveltimes for infrasonic waves propagating in a stratified atmosphere, *Geophys. J. Int.*, *135*(1), 255–263.
- Georges, T. M. (1968), Collisional interaction of atmospheric waves with the ionospheric F region, in *Acoustic-Gravity Waves in the Atmosphere*, vol. 1, edited by T. M. Georges, 377 pp., U.S. Gov. Print. Off., Washington, D. C.
- Georges, T. M., and W. H. Hooke (1970), Wave-induced fluctuations in ionospheric electron content: A model indicating some observational biases, *J. Geophys. Res.*, *75*(31), 6295–6308, doi:10.1029/JA075i031p06295.
- Heki, K., and J. Ping (2005), Directivity and apparent velocity of the coseismic ionospheric disturbances observed with a dense GPS array, *Earth Planet. Sci. Lett.*, *236*(3–4), 845–855, doi:10.1016/j.epsl.2005.06.010.
- Hooke, W. H. (1968), Ionospheric irregularities produced by internal atmospheric gravity waves, *J. Atmos. Terr. Phys.*, *30*(5), 795–823, doi:10.1016/S0021-9169(68)80033-9.
- Hunsucker, R. D., and J. K. Hargreaves (2002), *The High-Latitude Ionosphere and its Effects on Radio Propagation*, Cambridge Univ. Press, Cambridge.
- Lognonné, P., E. Clévéde, and H. Kanamori (1998), Computation of seismograms and atmospheric oscillations by normal-mode summation for a spherical earth model with realistic atmosphere, *Geophys. J. Int.*, *135*(2), 388–406.
- Lognonné, P., R. Garcia, F. Crespon, G. Occhipinti, A. Kherani, and J. Artru-Lambin (2006), Seismic waves in the ionosphere, *Europhys. News*, *37*(4), 11–15.
- Mannucci, A. J., B. D. Wilson, and C. D. Edwards (1993), A new method for monitoring the Earth's ionospheric total electron content using the GPS global network, in *Proceedings of the 6th International Technical Meeting of the Satellite Division of the Institute of Navigation (ION GPS 1993)*, pp. 1323–1332, Salt Palace Convention Center, Salt Lake City, Utah.
- Occhipinti, G., P. Dorey, T. Farges, and P. Lognonné (2010), Nostradamus: The radar that wanted to be a seismometer: IONOSPHERIC SEISMOLOGY, *Geophys. Res. Lett.*, *37*, L18104, doi:10.1029/2010GL044009.
- Occhipinti, G., L. Rolland, P. Lognonné, and S. Watada (2013), From Sumatra 2004 to Tohoku-Oki 2011: The systematic GPS detection of the ionospheric signature induced by tsunamigenic earthquakes, *J. Geophys. Res. Space Physics*, *118*, 3626–3636, doi:10.1002/jgra.50322.
- Picone, J. M., A. E. Hedin, D. P. Drob, and A. C. Aikin (2002), NRLMISE-00 empirical model of the atmosphere: Statistical comparisons and scientific issues, *J. Geophys. Res.*, *107*(A12), 1468, doi:10.1029/2002JA009430.
- Rolland, L. M., P. Lognonné, and H. Munekane (2011), Detection and modeling of Rayleigh wave induced patterns in the ionosphere, *J. Geophys. Res.*, *116*, A05320, doi:10.1029/2010JA016060.
- Rost, S., and C. Thomas (2002), Array seismology: Methods and applications, *Rev. Geophys.*, *40*(3), 1008, doi:10.1029/2000RG000100.